Advanced Materials

ADVANCED MATERIALS
www.advmat.de

RESEARCH ARTICLE

Precision-Engineered Electronic Modulation of Ruthenium Clusters and Single Atoms on Vacancy-Rich α-MoC_{1-x} Enables Efficient Electrocatalytic Water Splitting

Jixin Yao[1] | Jie Wang[2] | Wen Wang[3] | Haifeng Xu[4] | Dongmeng Chen[5] | Guang Li[2] | Zhong Jin[6]

[1]Anhui Province Key Laboratory of Simulation Calculation and Design for Electronic Information System, College of Electronic Information and Integrated Circuits, Hefei Normal University, Hefei, Anhui, P. R. China | [2]School of Materials Science and Engineering, Anhui Key Laboratory of Information Materials and Devices, Key Laboratory of Structure and Functional Regulation of Hybrid Materials of Ministry of Education, Anhui University, Hefei, Anhui, P. R. China | [3]School of Electronic Engineering, Chaohu University, Chaohu, Hefei, P. R. China | [4]School of Electronic Information Engineering, Hefei Institute of Technology, Hefei, Anhui, P. R. China | [5]College of Science, China University of Petroleum, Qingdao, China | [6]State Key Laboratory of Coordination Chemistry, MOE Key Laboratory of Mesoscopic Chemistry, MOE Key Laboratory of High Performance Polymer Materials and Technology, Jiangsu Key Laboratory of Clean Energy Catalysis and Intelligent Green Chemical Engineering, Suzhou Key Laboratory of Green Intelligent Manufacturing of New Energy Materials and Devices, Tianchang New Materials and Energy Technologies Research Center, Institute of Green Chemistry and Engineering, School of Chemistry and Chemical Engineering, Nanjing University, Nanjing, Jiangsu, P. R. China

Correspondence: Wen Wang (063029@chu.edu.cn) | Haifeng Xu (xuhaifeng@ahszu.edu.cn) | Zhong Jin (zhongjin@nju.edu.cn)

Received: 9 October 2025 | **Revised:** 28 November 2025 | **Accepted:** 16 December 2025

Keywords: electrocatalytic mechanism | hydrogen evolution reaction | Ru clusters | Ru single atoms | Zn–H_2O batteries

ABSTRACT

Maximizing the utilization of active metals while maintaining efficient catalytic activity is of great importance for electrocatalytic alkaline hydrogen evolution reaction. Herein, we report a facile pyrolysis strategy to anchor Ru clusters and adjacent Ru single atoms on α-MoC_{1-x} coated carbon nanospheres (termed as $Ru_{CS/SA}$/α-MoC_{1-x}/C). Theoretical calculations combined with in situ characterizations reveal that an electron-bridging mechanism whereby Ru single atoms donate electrons to the defective α-MoC_{1-x}, which subsequently transfers electron to Ru clusters, enabling a cooperative modulation of the electronic structure across different types of Ru sites. Therefore, the dual excitation of Ru single atoms and α-MoC_{1-x} weakens the binding strength between Ru clusters and H*, accelerates the desorption of H_2. The as-obtained 3%-$Ru_{CS/SA}$/α-MoC_{1-x}/C sample attains an excellent overpotential of 9 mV at 10 mA cm^{-2} along with a mass activity of 20.38 A mg^{-1}_{Ru} (-100 mV) and a turnover frequency of 1.71 H_2 s^{-1} at 25 mV, which is larger than those of 20% Pt/C. Moreover, Both the anion exchange membrane water electrolysis cells and Zn–H_2O batteries employing 3%-$Ru_{CS/SA}$/α-MoC_{1-x}/C as the cathode electrocatalyst exhibit exceptional performance.

1 | Introduction

Hydrogen energy, as one of the greenest energy sources with the greatest potential to replace fossil fuels, is of great significance for reducing air pollution and mitigating climate change [1–3]. Currently, the electrocatalytic hydrogen evolution reaction (HER) is considered as the cleanest hydrogen production technology [4, 5], which can sustainably produce hydrogen (H_2) using green electricity from renewable sources including solar, wind, and tidal. As a critical industrial method to produce high-purity hydrogen economically and sustainably, alkaline HER has emerged as a focal point of extensive scientific investigation. However, the hydrogen generation efficiency of alkaline HER is lower than that of acidic HER, mainly because of the additional Volmer step ($H_2O + e^- \rightarrow H_{ad} + OH$), which is considered the rate-determining step for alkaline HER [6–8]. Despite significant

advances in noble metal Pt-based catalysts for alkaline HER, their high cost remains a critical barrier to practical application. Therefore, it is crucial to develop efficient and inexpensive catalysts for alkaline HER. Ruthenium (Ru), costing only ≈30% of platinum while exhibiting comparable water binding energy to Pt, emerges as an ideal substitute for Pt in the HER [9–11]. To date, while Ru-based electrocatalysts have demonstrated remarkable advancements in acidic HER, their catalytic activity in alkaline HER remains critically constrained by sluggish water dissociation, thereby yielding subpar performance [12, 13]. The underlying challenge resides in inadequate proton availability, rooted in sluggish H_2O dissociation and robust adsorption of generated OH* during the Volmer step. These factors synergistically induce catalyst poisoning [14–16]. Hence, the rational design of efficient Ru-based electrocatalysts for alkaline HER to rival the performance of acidic HER represents a critical challenge.

Recently, He et al. revealed that Ru single atoms incorporated into the nickel-vacancy caused localized structural polarization of Ru sites, reducing the dissociation energy of water and improving free energy of hydrogen adsorption. This combination obtained 54 mV at 10 mA cm^{-2} for an alkaline HER [17]. Additionally, Hu et al. discovered that the electronic structure of Ru clusters is size-dependent: 1 nm Ru clusters exhibit superior H_2O dissociation capacity and upward-shifted *d*-band centers compared to Ru single atoms, while 3 nm Ru clusters show enhanced HER activity attributed to optimized hydrogen adsorption-desorption kinetics [12]. Further insights from Zhang et al. proposed that electrochemical triggering of Ru cluster regeneration on $LaRuSi_3$ surfaces induces optimized charge delocalization, thereby facilitating water adsorption-dissociation at Ru active sites while enhancing electrical conductivity and electrochemical surface area [18]. These findings jointly reveal the unique size effect and interface regulation mechanism of ruthenium-based materials in alkaline HER. In view of this, we speculate that Ru clusters combined with single atoms may be more conducive to dissociation of water. Nevertheless, the problems such as OH* poisoning and the easy tendency of individual atoms to agglomerate into larger clusters remain enormous challenges.

Numerous studies have demonstrated that suitable supports not only anchor metal atoms/clusters to inhibit agglomeration but also optimize the electronic structure of supported metals through strong metal–support interactions (SMSI) [19–22], thereby regulating OH* adsorption energy barriers to mitigate poisoning effects. Metal carbides own exceptional stability, outstanding conductivity and corrosion resistance. Additionally, carbon has a lower electronegativity compared to that of O, S, Se and P elements [6], which helps to optimize the electronic structure of Ru, allowing more d electrons to be involved in HER. Notably, α-MoC_{1-x} with abundant vacancies exhibits intrinsic HER activity and demonstrates remarkable potential. Furthermore, theoretical analyses show that α-MoC_{1-x} can significantly accelerate the Volmer step kinetics, thereby enhancing the HER rate [23, 24]. However, constrained by the synthetic challenges of α-MoC_{1-x}, exploratory research on utilizing it as a support to anchor Ru single atoms and clusters remains extremely scarce. This directly results in the synergistic mechanisms between them yet to be clarified.

Herein, we report a facile pyrolysis strategy enabling the anchoring of Ru clusters and adjacent single atoms onto α-MoC_{1-x} supports. Benefiting from the spatial confinement and protective effects of the carbon framework, α-MoC_{1-x} nanocrystals with an approximate size of 5 nm are tightly encapsulated within the carbon matrix. The vacancy-rich α-MoC_{1-x}, functioning as a distinctive support, not only stabilizes the Ru single atoms and clusters (designated as $Ru_{CS/SA}/\alpha$-MoC_{1-x}/C) but also directly participates in charge redistribution via its abundant defect sites. The high-angle annular dark-field scanning transmission electron microscopy (HAADF-STEM) results demonstrate that Ru clusters and single atoms are successfully anchored on α-MoC_{1-x}. Density functional theory (DFT) calculations for the first time predict an electronic bridging mechanism, wherein Ru single atoms donate electrons to defective α-MoC_{1-x}, which subsequently transfers electrons to Ru clusters, thereby enabling the synergistic modulation of the electronic structures of different types of Ru sites. This complementary mechanism is further corroborated by XPS and XAFS analyses, which validate the opposite charge transfer directions between single atoms and clusters as predicted by DFT. Furthermore, by systematically varying the ruthenium loading, we determine that 3% constitutes the optimal composition ratio for the balanced coexistence of single atoms and clusters. The as-prepared 3%-$Ru_{CS/SA}/\alpha$-MoC_{1-x}/C displays an overpotential of 9 mV at 10 mA cm^{-2}, a mass activity of 20.38 A mg^{-1} Ru, and a TOF of 1.71 s^{-1} at 25 mV in alkaline solution. These values are significantly greater than those of 20% Pt/C catalysts. Meanwhile, using 3%-$Ru_{CS/SA}/\alpha$-MoC_{1-x}/C as the cathodic catalyst, the anion exchange membrane water electrolysis (AEMWE) cells maintained a current density of 1.0 A cm^{-2} for 550 h. Additionally, 3%-$Ru_{CS/SA}/\alpha$-MoC_{1-x}/C is used to construct Zn–H_2O batteries in the 1 M KOH, enabling continuous operation for electricity generation. The constructed battery reaches up to 22.50 mW cm^{-2} and achieves sustainable discharge at 10 mA cm^{-2} for 20 h, attributed to the exceptional alkaline HER performance of 3%-$Ru_{CS/SA}/\alpha$-MoC_{1-x}/C catalysts. This work not only effectively enhances the catalyst's catalytic activity at the atomic level via the reverse capture strategy, but also opens more opportunities for building efficient AEMWE cells and Zn–H_2O batteries.

2 | Results and Discussion

2.1 | Theoretical Prediction

Previous research shows that α-MoC_{1-x} has face-centered cubic (fcc) structure (hexoctahedral (*Fm*3_*m*) space group) [25], which is structurally similar to Pt and Ru metal. Driven by SMSI, Pt and Ru possess the capability to capture electrons, which is very beneficial for reduction reactions [26–28]. As a demonstration, α-MoC_{1-x} anchored with Ru single atoms, Ru clusters, and (both Ru single atoms and clusters) are selected as models. The performance of HER is preliminarily verified through DFT calculations. The above corresponding theoretical models, which provides crucial insights and detailed information, are clearly shown in (Figures S1–S3). The catalyst models (Figure S4) with three different spacing distances (5.13, 7.20, and 9.93 Å) correspond to hydrogen adsorption energies of -0.54, -0.37, and -0.56 eV, respectively. The detailed description is included in the Supporting Information. According to the above structural

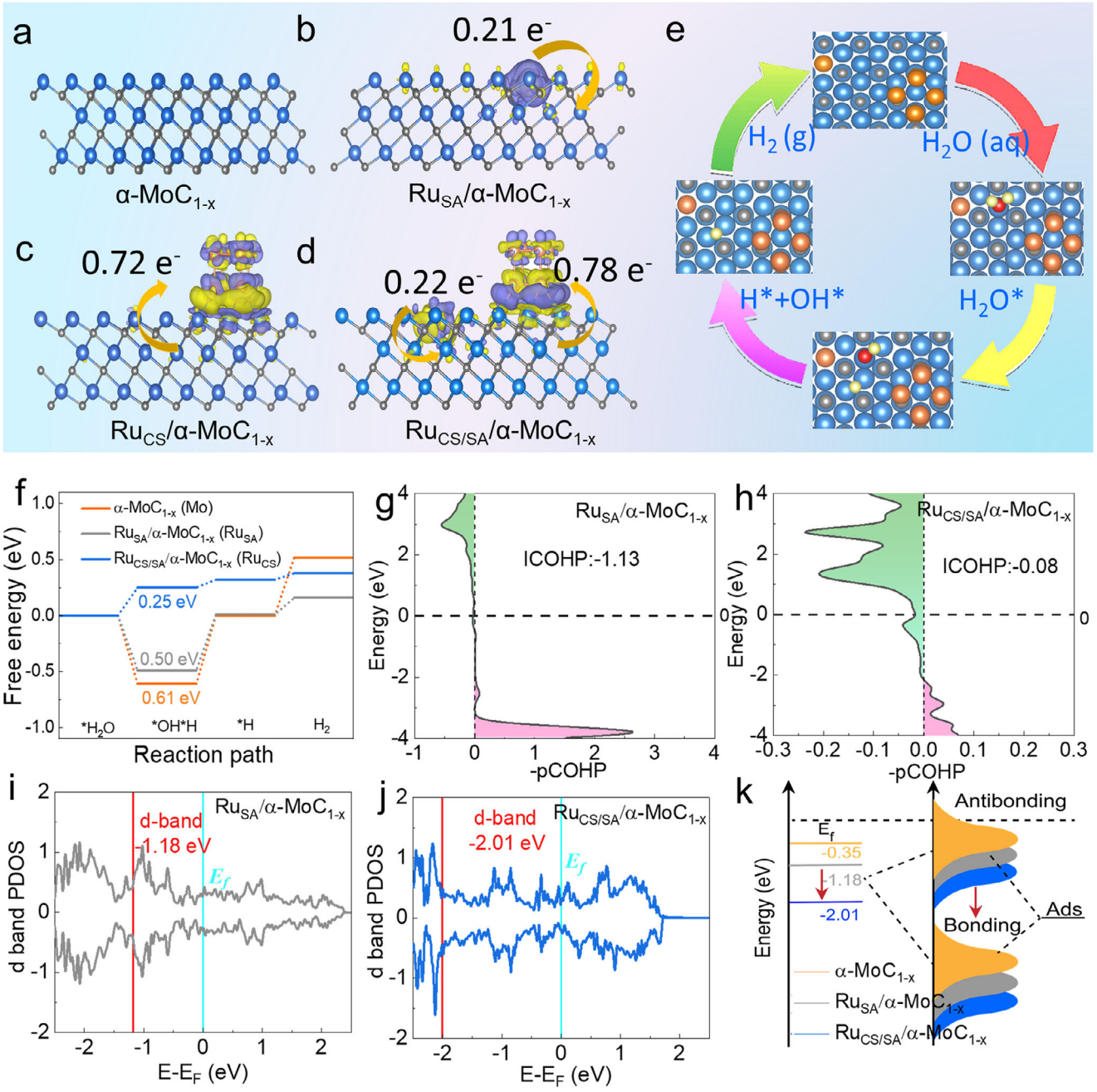

FIGURE 1 | a–d) The differential charge density of α-MoC_{1-x}, Ru_{SA}/α-MoC_{1-x}, Ru_{CS}/α-MoC_{1-x} and $Ru_{CS/SA}/\alpha$-MoC_{1-x} (Isosurface unit is 0.007 eÅ, the light blue, gray and orange ball represent the Mo, C and Ru, respectively). e) The intermediate products of the primary reaction steps. f) Reaction energy profiles of the complete HER reaction on the α-MoC_{1-x}, Ru_{SA}/α-MoC_{1-x} and $Ru_{CS/SA}/\alpha$-MoC_{1-x}/C models. g and h) The ICOHP values of Ru_{SA}/α-MoC_{1-x} and $Ru_{CS/SA}/\alpha$-MoC_{1-x}. i,j) The *d*-band PDOS of Ru_{SA}/α-MoC_{1-x} and $Ru_{CS/SA}/\alpha$-MoC_{1-x}/C. k) The d-band centers of the α-MoC_{1-x}, Ru_{SA}/α-MoC_{1-x} and $Ru_{CS/SA}/\alpha$-MoC_{1-x}/C.

analysis, the charge density difference resulting from the metal-support interaction was obtained. The observation of the electron distribution is depicted in Figure 1a–d. It clearly shows the significant distribution of the electron cloud at the interface. The purple electron cloud indicates the dissipation of electrons, while the yellow electron cloud means the accumulation of electrons. The pure α-MoC_{1-x} model is shown in Figure 1a. It is worth noting that Ru single atoms are in a state of losing electrons (0.21 e^-) on α-MoC_{1-x}, which is displayed in Figure 1b. Moreover, Ru clusters obtain a total of 0.72 e^- based on the α-MoC_{1-x} substrate (Figure 1c). Ru single atoms and clusters are co-embedded in the α-MoC_{1-x} model to investigate the charge transfer and distribution among the three components. It can be found that Ru clusters gain 0.78 e^- from the Ru single atom and α-MoC_{1-x} substrate, which is 0.06 e^- more than the charge gain (0.72 e^-) of pure Ru clusters anchored on α-MoC_{1-x}. The detailed situation of electron transfer for Ru single atom, Ru cluster and α-MoC_{1-x} is displayed in Figure 1d. Based on comprehensive analysis, we can infer that the synergistic anchoring effect of Ru single atoms and clusters on α-MoC_{1-x} leads to α-MoC_{1-x} extracting approximately

0.22 e^- from Ru single atoms, inducing the reconstruction of the surface electronic structure. This in turn enhances the ability of Ru clusters to acquire electrons from α-MoC_{1-x}, ultimately contributing to a more electron-enriched state on the surface of Ru clusters. Therefore, it is highly beneficial for the HER process. To gain a deeper insight into HER kinetics, the intermediate products of the primary reaction steps (Figure 1e) were calculated [29]. As presented in Figure 1f, the energy barrier of the Volmer reaction ($H_2O^*+e^-\rightarrow H^*+OH^-$) for $Ru_{CS/SA}$/α-MoC_{1-x}/C (Ru_{CS}) is 0.25 eV, which is lower than Ru_{SA}/α-MoC_{1-x}/C (Ru_{SA}, 0.50 eV) and α-MoC_{1-x}/C (Mo, 0.61 eV), implying $Ru_{CS/SA}$/α-MoC_{1-x}/C (Ru_{CS}) has a stronger ability for water dissociation and the formation of H* on Ru clusters [30]. The Ab initio molecular dynamics (AIMD) theoretical simulation and detailed analysis are displayed in Figure S5. Besides, the H desorption energy barrier (0.06 eV) of $Ru_{CS/SA}$/α-MoC_{1-x}/C (Ru_{CS}) is lower than that of Ru_{SA}/α-MoC_{1-x}/C (Ru_{SA}, 0.15 eV) and α-MoC_{1-x} (Mo, 0.52 eV), suggesting that Ru clusters accelerate the rate-determining step (Tafel reaction) under the dual action of Ru single atoms and the α-MoC_{1-x} substrate in alkaline conditions. The performance of ΔG_{*OH*H} for $Ru_{CS/SA}$/α-MoC_{1-x}/C (Ru_{CS}) is superior to that of Ru_{SA}/α-MoC_{1-x}/C (Ru_{SA}) and α-MoC_{1-x}/C (Mo), revealing the greater H* and OH* desorption ability. The results of the limiting potential (Figure S6) indicate that the Ru clusters have the lowest limiting potential (0.62 eV) compared to Ru_{SA}/α-MoC_{1-x}/C (Ru_{SA}, 0.99 eV) and α-MoC_{1-x}/C (Mo, 1.22 eV). This means that the Ru clusters are more likely to undergo a HER catalytic reaction. At the catalyst sites, the obtained *E*ads(H_2O*) values are shown in Figure S7, which are -1.09 eV for α-MoC_{1-x}, -0.99 eV for Ru_{SA}/α-MoC_{1-x} and -0.90 eV for $Ru_{CS/SA}$/α-MoC_{1-x}. All three values are negative, indicating that water is spontaneously adsorbed on these active sites. The order of adsorption strength is α-MoC_{1-x} > Ru_{SA}/α-MoC_{1-x} > $Ru_{CS/SA}$/α-MoC_{1-x}. Moderate water adsorption is conducive to initiating the interfacial Volmer step, while preventing active site blockage caused by excessively strong adsorption. To further comprehend the influence of Ru single atoms and clusters, crystal orbital Hamilton population (COHP) analysis was executed to study the bonding strength between active sites and the H* intermediate [31]. Therefore, we can make a reasonable inference that the weak binding between such active sites and adsorbed intermediates is caused by the change in the electron distribution state of the catalyst. As shown in Figure 1g,h and Figure S8, the order of ICOHP values is α-MoC_{1-x} (-1.51) < Ru_{SA}/α-MoC_{1-x} (-1.03) < $Ru_{CS/SA}$/α-MoC_{1-x} (-0.08). According to the ICOHP theory, a less negative ICOHP value indicates weaker bonding strength. Thus, $Ru_{CS/SA}$/α-MoC_{1-x} exhibits the weakest bonding strength. Due to the weak interaction between MoC-Ru and the H* intermediate, the formation of H_2 at the cluster site is very beneficial. Therefore, projected density of states (PDOS) analysis was also conducted to clarify the electronic distribution characteristics of the active centers. As shown in Figure 1i,j and Figure S9, compared with Ru_{SA}/α-MoC_{1-x} and α-MoC_{1-x}, the d-band center of the active sites in $Ru_{CS/SA}$/α-MoC_{1-x} is farther from the Fermi level (E_f). The d-band variation diagram is clearly shown in Figure 1k. This electronic distribution phenomenon indicates that the adsorption strength of reaction intermediates can be optimized by adjusting the electronic distribution state of the catalyst's *d*-band center. In addition, the comparison of Gibbs free energy for H* adsorption and COHP among $Ru_{CS/SA}$/α-MoC_{1-x}, Ru_{SA}/α-MoC_{1-x}, and α-MoC_{1-x} strongly confirms this point [32]. Consequently, this weakens the adsorption of H* and significantly promotes the Tafel process in the hydrogen evolution process. The theoretical results show that the synergistic effect of co-embedding Ru clusters and Ru single atoms with α-MoC_{1-x} can enhance Ru cluster HER activity.

2.2 | Preparation and Characterizations of X%-$Ru_{CS/SA}$/α-MoC_{1-x}/C Samples

The preparation steps of $Ru_{CS/SA}$/α-MoC_{1-x}/C samples were schematically illustrated in Figure 2a. Briefly, dopamine and ammonium molybdate were complexed to form the Mo-precursor in a water-alcohol mixed solution in the presence of ammonia, and α-MoC_{1-x}/C was formed via high-temperature calcination. α-MoC_{1-x}/C was used as a carrier to capture ruthenium by impregnation, followed by thermal reduction in 10% H_2/Ar to form the x%-$Ru_{CS/SA}$/α-MoC_{1-x}/C (x% represents Ru content). The X-ray diffraction (XRD) patterns (Figure 2b) of x%-$Ru_{CS/SA}$/α-MoC_{1-x}/C and α-MoC_{1-x}/C demonstrate all the diffraction peaks. The Ru content was determined by inductively coupled plasma atomic emission spectroscopy (ICP-AES) analysis, as shown in Table S1. What is noteworthy is that the characteristic peak centered at 24.81° is generated by the (002) crystal plane of the carbon substrate. A series of diffraction peaks from α-MoC_{1-x} occurred at 36.41°, 42.29°, 61.35°, and 73.49°, and perfectly match the (111), (200), (220), and (311) facets, respectively. Therefore, the given α-MoC_{1-x} is cubic structure with JCPDS 89–2868 [33]. As can be seen, the X-ray diffraction (XRD) pattern of 3%-$Ru_{CS/SA}$/α-MoC_{1-x}/C is similar to that of crystal structure of the pure α-MoC_{1-x}/C, signifying that the atomic Ru was well incorporated into the α-MoC_{1-x} crystal lattice and has a very good match with its lattice [34]. As described in Figures S10–S13, the holistic morphology of the synthesized x%-$Ru_{CS/SA}$/α-MoC_{1-x}/C from scanning electron microscopy (SEM) and transmission electron microscopy (TEM) displays a hierarchical spherical solid structure, which is almost in agreement with that of the pure α-MoC_{1-x}/C (Figure S14). To characterize the microstructure of the as-synthesized samples, the TEM and SEM were employed for morphological analysis. Significantly, the tiny α-MoC_{1-x} nanocrystals (around 5 nm) were wrapped and encapsulated in the carbon matrix, which are displayed in (Figure 2c,d). α-MoC_{1-x} nanocrystals are designated by the pink circles; the blue range represents the carbon layer, which is displayed in (Figure S15). Subsequently, HAADF-STEM was applied to characterize α-MoC_{1-x} nanocrystals. As depicted in Figure S16, the analysis resolved two distinct sets of continuous lattice fringes with interplanar spacings of 2.03 and 2.34 Å-assignable to the (111) and (200) planes of α-MoC_{1-x}, respectively, forming a 54.71° plane angle. Furthermore, 3%-$Ru_{CS/SA}$/α-MoC_{1-x}/C was also characterized at the atomic scale using HAADF-STEM (Figure 2e), which exhibits two distinct HAADF signal intensities—a phenomenon inherently linked to atomic mass contrast, where Ru atoms appear brighter than Mo atoms due to their higher atomic number. Therefore, Ru species are easily identified in 3%-$Ru_{CS/SA}$/α-MoC_{1-x}/C (Ru clusters are specified by the green circles; Ru single atoms are identified by the yellow circles). The selected (1) white areas for 3%-$Ru_{CS/SA}$/α-MoC_{1-x}/C are enlarged in equal proportion, which is exhibited in Figure 2f. It is evident that Ru clusters and Ru single atoms on α-MoC_{1-x} lattice. The elemental mapping (Figure 2h–k) from the selected region (Figure 2g) emerges the uniform distribution of Ru, Mo, C atoms, which can strongly confirm the Ru clusters

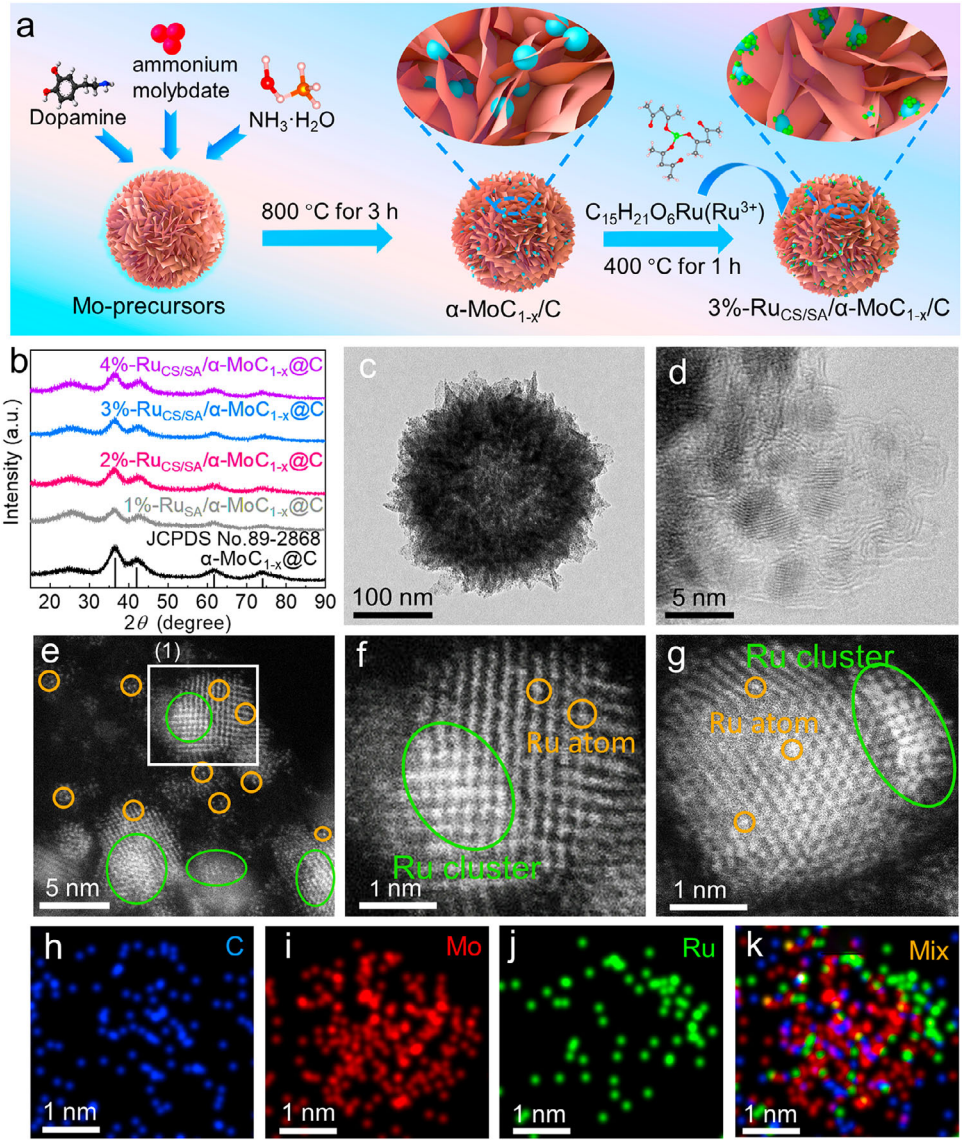

FIGURE 2 | a) Schematic diagram for the synthesis of 3%-$Ru_{CS/SA}$/α-MoC_{1-x}/C. (pink, blue, and green ball corresponding to the C, Mo and Ru elements, respectively). b) XRD of x%-$Ru_{CS/SA}$/α-MoC_{1-x}/C. c, d) TEM and HAADF-STEM images of the α-MoC_{1-x}/C at different scales. e,f) HAADF-STEM images of the 3%-$Ru_{CS/SA}$/α-MoC_{1-x}/C at different scales. g) The selected electron diffraction range image. h–j) The elemental mapping images of 3%-$Ru_{CS/SA}$/α-MoC_{1-x}/C and k) the overlap elemental image of C, Ru and Mo.

and single atoms loaded on the surface of α-MoC_{1-x}, and disclose the feasibility of $Ru_{CS/SA}$/α-MoC_{1-x}/C synthesis method. For comparison, 1%-Ru_{SA}/α-MoC_{1-x}/C, 2%-$Ru_{CS/SA}$/α-MoC_{1-x}/C and 4%-$Ru_{CS/SA}$/α-MoC_{1-x}/C are also shown in (Figures S17–S19).

2.3 | Electrocatalytic Performance Measurements

The HER performance of 3%-$Ru_{CS/SA}$/α-MoC_{1-x}/C and that of series contrast samples were conducted using a three-electrode electrochemical cell with linear sweep voltammetry (LSV) in 1 M KOH solution. The α-MoC_{1-x}/C-n (n represents C content) series samples for the correlation test are displayed in (Figures S20–S22). The best proportion among the α-MoC_{1-x}/C-n series samples is selected and named α-MoC_{1-x}/C. Meanwhile, as illustrated in Figure 3a, the LSV curves indicate that 3%-$Ru_{CS/SA}$/α-MoC_{1-x}/C exhibits overpotentials of 9 mV (10 mA cm^{-2}) and 58 mV (100 mA cm^{-2}), respectively. As expected, this result is better than other given samples {(2%-$Ru_{CS/SA}$/α-MoC_{1-x}/C is 36 mV and 103 mV), (4%-$Ru_{CS/SA}$/α-MoC_{1-x}/C is 16 mV and 86), (Ru/C is 78 mV and 176 mV) and Pt/C is 40 and 136 mV)} under the same condition. The above values are presented in Figure 3b. Meanwhile, the reaction kinetics are evaluated based on the Tafel slope obtained from the transformed LSV curve. As illustrated in Figure 3c, 3%-$Ru_{CS/SA}$/α-MoC_{1-x}/C displays a low Tafel slope of only 31.25 mV dec^{-1}, outperforming 2%-$Ru_{CS/SA}$/α-MoC_{1-x}/C (39.11 mV dec^{-1}), 4%-$Ru_{CS/SA}$/α-MoC_{1-x}/C (32.83 mV dec^{-1}), Pt/C (40.07 mV dec^{-1}), and Ru-C (70.24 mV dec^{-1}). This indicates that 3%-$Ru_{CS/SA}$/α-MoC_{1-x}/C catalyst adheres to the rapid Volmer-Tafel mechanism. The double-layer capacitance (C_{dl}) values (Figures S23 and S24) are measured to evaluate the exposed active sites of the catalyst. Significantly, 3%-$Ru_{CS/SA}$/α-MoC_{1-x}/C has a C_{dl} of 47.22 mF cm^{-2}, far exceeding that of 2%-$Ru_{CS/SA}$/α-MoC_{1-x}/C (40.11 mF cm^{-2}), 4%-$Ru_{CS/SA}$/α-MoC_{1-x}/C

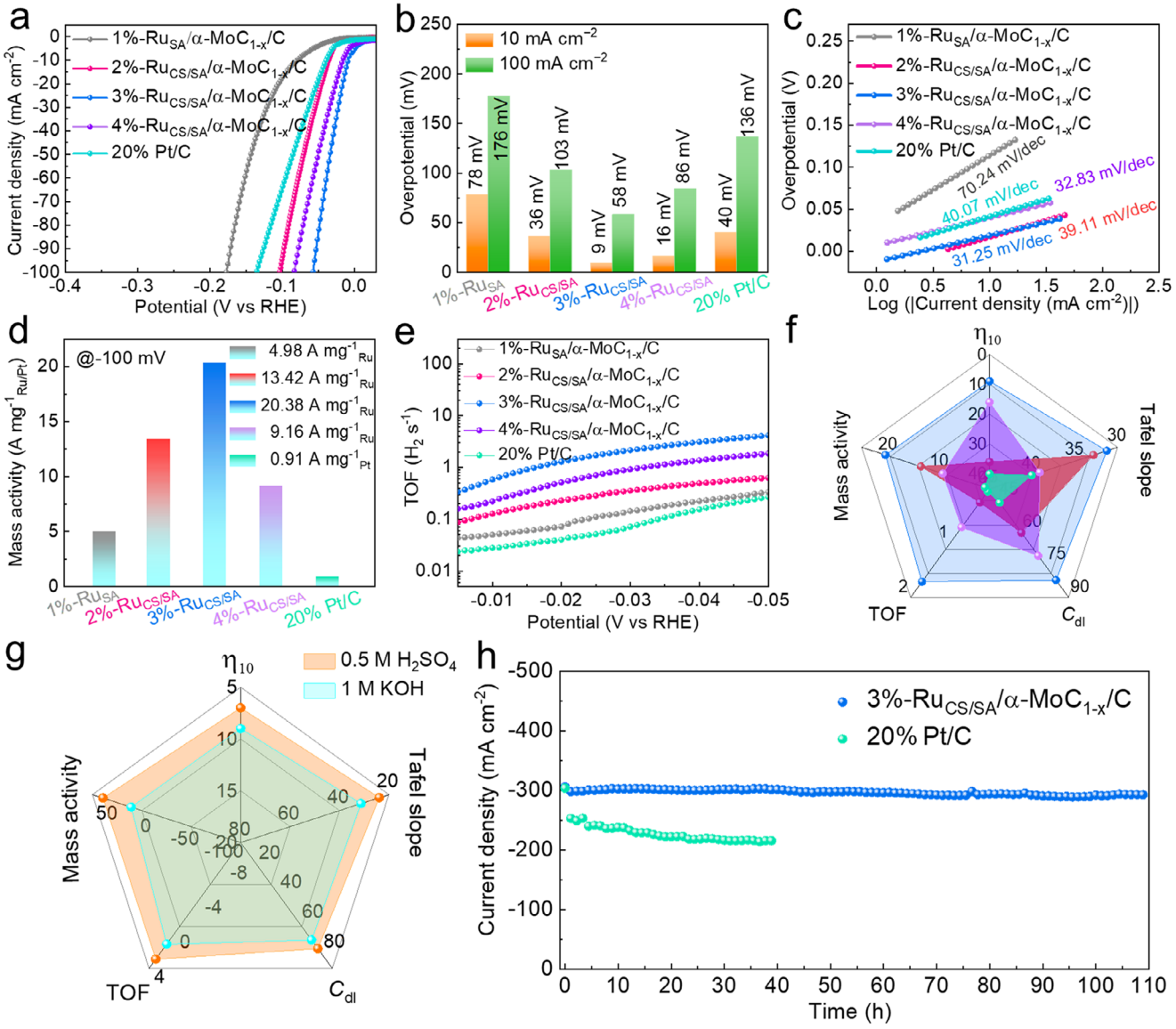

FIGURE 3 | a) polarization curves of 3%-$Ru_{CS/SA}$/α-MoC_{1-x}/C in comparison with 20 wt% Pt/C and other samples with various Ru loading. b) Overpotential at the current density of 10 mA cm^{-2} and 100 mA cm^{-2}, c) Tafel plots derived from the corresponding HER polarization curves. d) the mass activity at -100 mV (vs RHE) with respect to the reference samples. e) TOFs curves with respect to the reference samples. (the different Ru loading). f) Comparison for HER performance metrics for x%-$Ru_{CS/SA}$/α-MoC_{1-x}/C (where x% represents the Ru loading ratios of 2%, 3%, or 4%) and commercial Pt/C electrocatalysts. g) Comparison for HER performance metrics for 3%-$Ru_{CS/SA}$/α-MoC_{1-x}/C under alkaline electrolyte and acid electrolyte (0.5 M H_2SO_4). h) The chronoamperometry test (*I*–*T*) of 3%-$Ru_{CS/SA}$/α-MoC_{1-x}/C and 20% Pt/C at 300 mA cm^{-2}.

(45.32 mF cm^{-2}), and Pt/C (30.93 mF cm^{-2}), indicating that 3%-$Ru_{CS/SA}$/α-MoC_{1-x}/C exposes abundant reactive sites, leading to its superior activity. The Cu underpotential deposition (Cu-UPD) method was implemented (Figure S25) to determine the ECSA of 3%-$Ru_{CS/SA}$/α-MoC_{1-x}/C. The calculated ECSA of 3%-$Ru_{CS/SA}$/α-MoC_{1-x}/C is 1 cm^2, which is higher than that of other obtained samples. The mass activity and the TOF are equally important parameters, reflecting the utilization efficiency of noble metals and the intrinsic HER performance [14]. As illustrated in Figure 3d, 3%-$Ru_{CS/SA}$/α-MoC_{1-x}/C has a mass activity of 20.38 A mg^{-1}, surpassing 2%-$Ru_{CS/SA}$/α-MoC_{1-x}/C (13.42 A mg^{-1}) and 4%-$Ru_{CS/SA}$/α-MoC_{1-x}/C (9.16 A mg^{-1}). Notably, this value is 22.35 times greater than that of 20% Pt/C (0.91 A mg^{-1}). Additionally, the TOF (Figure 3e) is obtained to assess the catalytic efficiency of Ru in $Ru_{CS/SA}$/α-MoC_{1-x}/C. Typically, the TOF value of 1.71 H_2 s^{-1} for 3%-$Ru_{CS/SA}$/α-MoC_{1-x}/C at -25 mV, outperforming 2%-$Ru_{CS/SA}$/α-MoC_{1-x}/C (0.25 H_2 s^{-1}), 4%-$Ru_{CS/SA}$/α-MoC_{1-x}/C (0.71 H_2 s^{-1}) and 20% Pt/C (0.05 H_2 s^{-1}), indicating the superior catalytic efficiency of Ru in 3%-$Ru_{CS/SA}$/α-MoC_{1-x}/C. The comparison of the HER activity of 3%-$Ru_{CS/SA}$/α-MoC_{1-x}/C in alkaline solution (1 M KOH) with recently reported single-atom catalysts is presented in Table S2. The comprehensive performance comparison of the given contrast samples is presented in Figure 3f. The performance of 3%-$Ru_{CS/SA}$/α-MoC_{1-x}/C is optimal. Identification of the main active species is a critical step in analyzing the high performance of 3%-$Ru_{CS/SA}$/α-MoC_{1-x}/C. The detection of hydrogen desorption peaks and adsorption peaks is presented in Figure S26, these results experimentally demonstrate that the enhanced HER activity of 3%-$Ru_{CS/SA}$/α-MoC_{1-x}/C primarily stems from the optimal proportion of its Ru species. These Ru species serve as the true

hydrogen adsorption/desorption active sites. Meanwhile, the role of the α-MoC_{1-x} support is reflected in two aspects: stabilizing the Ru species and providing electronic interactions. To this end, potassium thiocyanate (KSCN) and ethylenediaminetetraacetic acid disodium (EDTA) were used to poison the catalyst [28, 35]. As shown in Figure S27, for α-MoC_{1-x}/C, SCN^- nearly eliminated HER activity, demonstrating that Mo sites are effectively suppressed. In contrast, in 3%-$Ru_{CS/SA}$/α-MoC_{1-x}/C, although the overall activity decreased significantly, a clear residual HER current remained, which can reasonably be attributed to Ru species. Considering the known stronger hydrogen affinity of Ru, this suggests that Ru clusters and single atoms are responsible for the observed residual activity. EDTA poisoning further supports this conclusion: it strongly affects dispersed Ru single atoms through chelation, while its influence on stable Ru clusters and lattice-embedded Mo is limited, leaving partial activity. Taken together, these results strongly support Ru as the primary contributor to the residual HER activity. Moreover, Combined characterization analysis using SCN^- and EDTA reveals that Ru single atoms and Ru clusters are anchored on the α-MoC_{1-x} lattice, with interactions existing among these three components. This structural feature is a key reason for the catalyst to exhibit excellent hydrogen evolution reaction (HER) performance. The HER performance in acidic media was further probed, with key kinetic parameters summarized in Figures S28–S34. The introduction of Ru single atoms and clusters modulates the hydrogen adsorption Gibbs free energy (Figure S35) from -0.52 eV to -0.06 eV. The closer this value approaches zero, the more efficiently it facilitates hydrogen adsorption/desorption, providing direct experimental validation that $Ru_{CS/SA}$/α-MoC_{1-x} under acidic conditions aligns with DFT predictions. The performance of the prepared catalysts and the relevant detailed discussion are presented in Figure S36, and the related tests were conducted in 1 M PBS (pH ≈ 7). To unravel the performance advantages of alkaline media, a comprehensive comparison of HER activity for 3%-$Ru_{CS/SA}$/α-MoC_{1-x}/C was conducted under acidic and alkaline conditions, as depicted in Figure 3g. Strikingly, 3%-$Ru_{CS/SA}$/α-MoC_{1-x}/C exhibits comparable HER performance in both alkaline and acidic media. This finding underscores the exceptional H_2O dissociation capability of 3%-$Ru_{CS/SA}$/α-MoC_{1-x}/C, which facilitates rapid hydrogen atom generation for subsequent HER elementary steps. Additionally, long-term stability serves as a critical metric for evaluating alkaline HER performance and gauging the catalyst's practical application potential. As shown in Figure 3h, both 3%-$Ru_{CS/SA}$/α-MoC_{1-x}/C and 20% Pt/C catalysts sustain 110 h of continuous operation at 300 mA cm^{-2}. Significantly, 3%-$Ru_{CS/SA}$/α-MoC_{1-x}/C demonstrates excellent catalytic stability, with the current density decay being negligible. Moreover, 3%-$Ru_{CS/SA}$/α-MoC_{1-x}/C exhibits superior catalytic stability compared to 20% Pt/C, as further validated by LSV measurements (Figure S37) after 5000 consecutive CV cycles. The results show a negligible overpotential shift of only 0.40 mV (increased by 0.40 mV), confirming the catalyst's exceptional durability. Furthermore, the electrolyte was analyzed using inductively coupled plasma optical emission spectrometry (ICP-OES). The results (as shown in Table S3) indicate that the concentrations of Mo ions in the electrolyte are 0.02 ppm and 0.06 ppm under the conditions of 100 and 1000 mA cm^{-2} for 100 h durability, respectively, demonstrating that the leaching of Mo species is negligible. The LSV curve of the pure carbon support is presented in (Figure S38), and it was compared with the LSV curves of α-MoC_{1-x}/C and $Ru_{CS/SA}$/α-MoC_{1-x}/C, respectively. The detailed description is included in the Supporting Information. HAADF-STEM (Figure S39) were performed before and after the HER tests. The statistical analysis indicates that the Ru nanoparticles exhibit an average particle size of 2.23 nm before the reaction and slightly increase to 2.42 nm after the reaction, confirming that the Ru species remain highly dispersed with only minor aggregation. The above comparison can well demonstrate the key role of the carbon support for durability.

2.4 | Mechanism Studies and In Situ Validations of 3%-$Ru_{CS/SA}$/α-MoC_{1-x}/C Electrocatalyst

Raman spectroscopy (Figure S40a) confirms the presence of graphitic carbon, with two distinct peaks corresponding to the D band (1350 cm^{-1}) and G band (1580 cm^{-1}). The I_D/I_G ratio can reflect the degree of defects generated at the edges of the carbon framework [36–38]. Notably, α-MoC_{1-x}/C and 3%-$Ru_{CS/SA}$/α-MoC_{1-x} /C exhibit highly consistent trends, indicating minimal structural or functional perturbation upon Ru incorporation. Furthermore, to determine the elemental composition and surface chemical states of the obtained materials, X-ray photoelectron spectroscopy (XPS) was employed. The Mo 3d XPS spectra (Figure S40b) of pristine α-MoC_{1-x}/C and 3%-$Ru_{CS/SA}$/α-MoC_{1-x}/C reveal three prominent peaks. The deconvolution of these peaks yields six components, assigned to Mo^{2+} (at 228.9 and 232.1 eV), Mo^{4+} (at 230.0 and 233.2 eV), and Mo^{6+} (at 232.1 and 235.3 eV) species, respectively. The C 1s XPS spectra (Figure S40c) reveals that there is an interaction between Mo and the carbon support, leading to the formation of Mo-C bonds. It should be noted that after Ru incorporation induces a positive shift in the Mo 3d binding energy and an increase in Mo^{6+} content. As shown in Figure 4a, compared to metallic Ru (Ru^0), the Ru 3p binding energy of the 1%-Ru_{SA}/α-MoC_{1-x}/C shifts toward higher energy levels, which is consistent with the electron donation behavior of Ru single atoms to the α-MoC_{1-x} support. In contrast, the Ru 3p binding energies of the 3%-$Ru_{CS/SA}$/α-MoC_{1-x}/C and 4%-$Ru_{CS/SA}$/α-MoC_{1-x}/C are closer to that of Ru^0 and shift toward lower energy levels, which aligns with the electron enrichment phenomenon of Ru clusters. Furthermore, compared with the 3%-$Ru_{CS/SA}$/α-MoC_{1-x}/C, the 4%-$Ru_{CS/SA}$/α-MoC_{1-x}/C exhibits a stronger dominance of Ru clusters. This stronger cluster dominance reduces the influence of Ru single atoms on 4%-$Ru_{CS/SA}$/α-MoC_{1-x}/C, thereby causing the Ru 3p binding energy of the 4%-$Ru_{CS/SA}$/α-MoC_{1-x}/C to deviate further from the characteristic binding energy of Ru^0 than that of the 3% Ru sample. This result is in excellent agreement with the charge transfer directions predicted by DFT calculations. To further confirm the interaction between ruthenium (Ru) and α-MoC_{1-x}, molybdenum (Mo)-free carbon-supported Ru was prepared as a control. As shown in Figure S41a, when Ru are anchored on the carbon matrix without Mo, the valence state of Ru is close to +3. The result of LSV curves (Figure S41b) suggest that the effect of Ru in 3%-Ru/C can be almost neglected. These indicates that the low valence state of Ru in $Ru_{CS/SA}$/α-MoC_{1-x}@C is closely associated with α-MoC_{1-x}. Notably, the deconvoluted Ru 3p peaks of 3%-$Ru_{CS/SA}$/α-MoC_{1-x}/C exhibit a slight negative shift relative to Ru^{3+}, approaching the binding energies of Ru/C (Ru^0), indicating that Ru species in the catalyst gain electrons from the α-MoC_{1-x} support [25, 39]. X-ray absorption spectroscopy

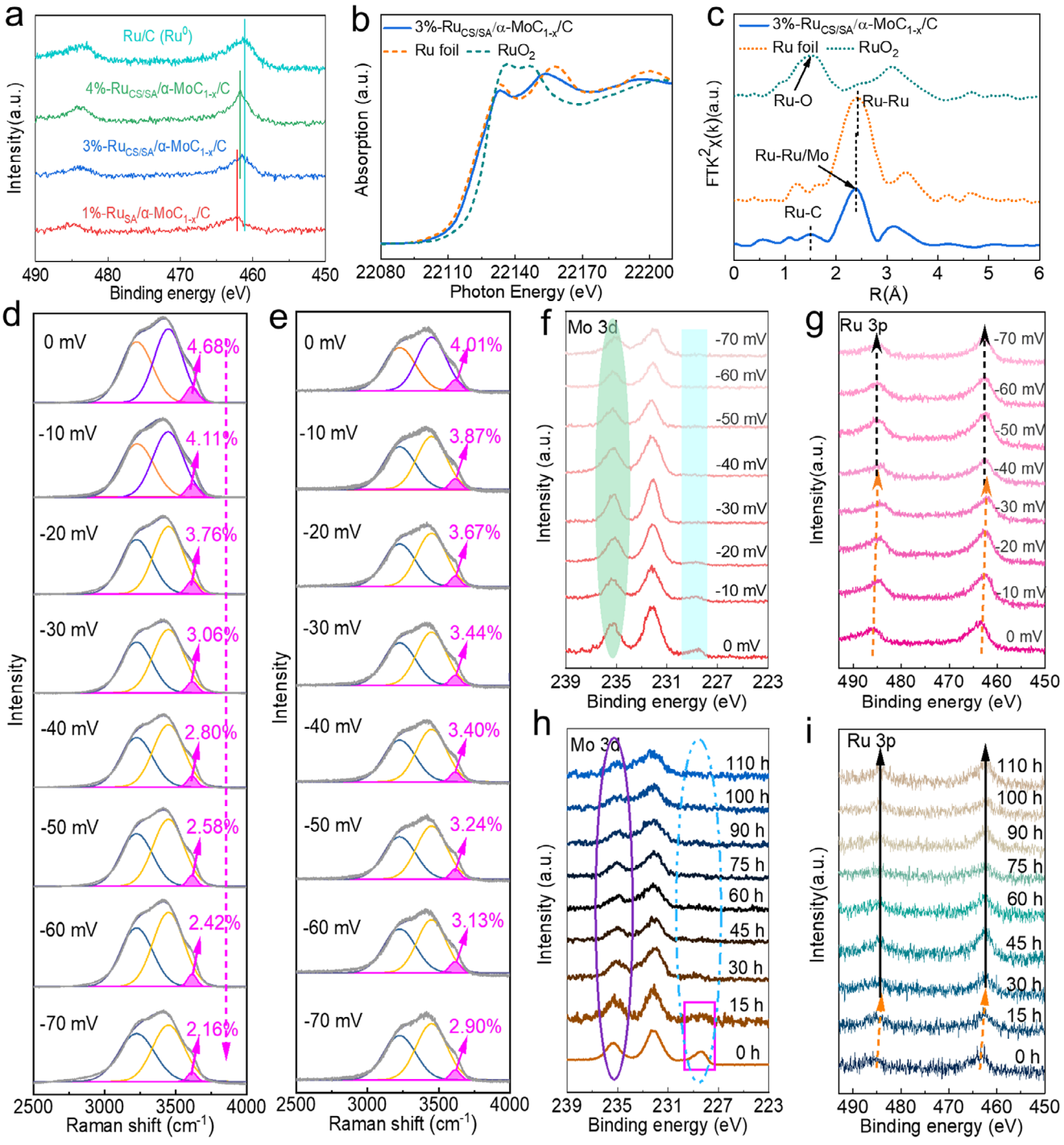

FIGURE 4 | a) Ru 3p spectra XPS patterns. b) Ru K-edge XANES spectra of 3%-$Ru_{CS/SA}$/α-MoC_{1-x}/C, Ru foil, and RuO_2. c) The corresponding Fourier transformed Ru K-edge EXAFS spectra. d) The operando Raman spectra of 1%-Ru_{SA}/α-MoC_{1-x}/C for interfacial water signals. e) The operando Raman spectra of 3%-$Ru_{CS/SA}$/α-MoC_{1-x}/C for interfacial water signals. f,g) Quasi-in situ Mo 3d and Ru 3p XPS spectra analysis of 3%-$Ru_{CS/SA}$/α-MoC_{1-x}/C for HER. h,i) Mo 3d and Ru 3p XPS spectra in different stages of the HER.

(XAS) was employed to probe the atomic coordination and electronic configuration of Ru species in 3%-$Ru_{CS/SA}$/α-MoC_{1-x}/C. During the sample preparation process, the boron nitride (BN) is sourced from XFNANO Materials. The Ru K-edge X-ray absorption spectra near-edge structure (XANES) spectra of 3%-$Ru_{CS/SA}$/α-MoC_{1-x}/C, Ru foil (metallic Ru^0), and RuO_2 (Ru^{3+}) are presented in Figure 4b, serving as references for valence state and coordination analysis. The 3%-$Ru_{CS/SA}$/α-MoC_{1-x}/C lies between Ru foil and RuO_2 in the spectrum, with a closer proximity to Ru foil, indicating that its Ru species exhibit metallic characteristics and an electron-rich state-consistent with XPS results [40]. The Ru K-edge XANES spectrum of 3%-$Ru_{CS/SA}$/α-MoC_{1-x}/C, located between those of Ru foil and RuO_2, shows a closer to Ru foil, indicating that Ru species maintain metallic characteristics with an electron-rich state. Furthermore, Ru K-edge Fourier-transformed EXAFS (Figure 4c) was performed to investigate the

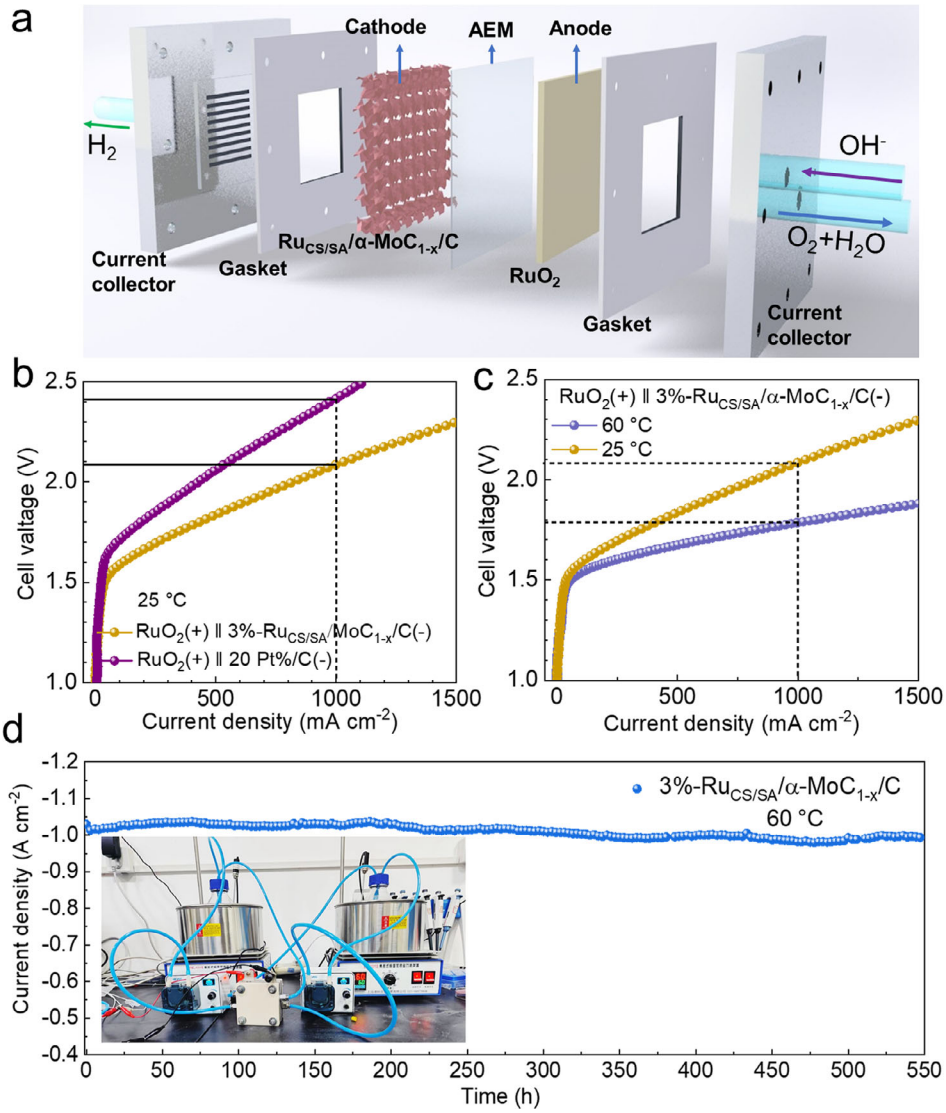

FIGURE 5 | a) Schematic diagram of an AEMWE device, and H_2 production by this AEMWE in alkaline media. b) Polarization curves of the AEMWE measured at 25°C using 3%-$Ru_{CS/SA}$/α-MoC_{1-x}/C and commercial 20% Pt/C as cathodic catalysts. c) Polarization curves of the AEMWE measured at 60°C and 25°C with 3%-$Ru_{CS/SA}$/α-MoC_{1-x}/C. d) The durability test of 3%-$Ru_{CS/SA}$/α-MoC_{1-x}/C at 60°C in the anion exchange membrane (AEM) based electrolyzer.

local coordination environment of Ru species in the catalyst. The Ru K-edge EXAFS spectrum of 3%-$Ru_{CS/SA}$/α-MoC_{1-x}/C features a main peak at 2.40 Å, assigned to Ru–Ru bonding in ultrafine Ru clusters, and a minor peak at 1.50 Å, attributed to Ru-C coordination from isolated Ru single atoms, confirming the coexistence of Ru single atoms and clusters. This structural assignment is in excellent agreement with HAADF-STEM observations. Notably, the Ru-Ru scattering intensity exceeds that of Ru-C, indicating that ultrafine Ru clusters constitute the predominant Ru species. The specific surface areas of 3%-$Ru_{CS/SA}$/α-MoC_{1-x}/C and α-MoC_{1-x}/C were characterized by Brunauer-Emmett-Teller (BET) analysis (Figure S42a). The specific surface areas of the two samples (3%-$Ru_{CS/SA}$/α-MoC_{1-x}/C and α-MoC_{1-x}/C) are nearly identical, demonstrating that Ru incorporation does not significantly affect the surface area. Integrating morphological and structural insights, the HER mechanism schematic of 3%-$Ru_{CS/SA}$/α-MoC_{1-x}/C in alkaline media is depicted in Figure S42b.

For alkaline HER, electrocatalytic performance hinges on the dissociation of water molecules to supply hydrogen atoms, with the Volmer step ($H_2O + e^- \rightarrow H^* + OH^-$) serving as the rate-determining process. Thus, catalysts must exhibit robust water adsorption capacity to lower the energy barrier for dissociation, a prerequisite for overcoming the sluggish kinetics of alkaline electrocatalysis. Therefore, in situ Raman measurements with stepwise potential (0 → -70 mV) were employed to assess the H_2O adsorption ability of the catalysts. Raman spectra (Figure 4d,e) reveal a broad peak at ≈3500 cm^{-1}, attributed to the O-H stretching vibration of adsorbed water at the catalyst-electrolyte interface. This assignment is consistent with the hydrogen bonding interactions between water molecules and active sites on the catalyst surface [41]. Three distinct peaks in the interfacial water region are centered at 3225 cm^{-1} (orange), 3450 cm^{-1} (purple), and 3615 cm^{-1} (pink), corresponding to different hydrogen bonding environments of adsorbed water molecules. Water molecules with trigonal and tetrahedral coordination in HER are generally

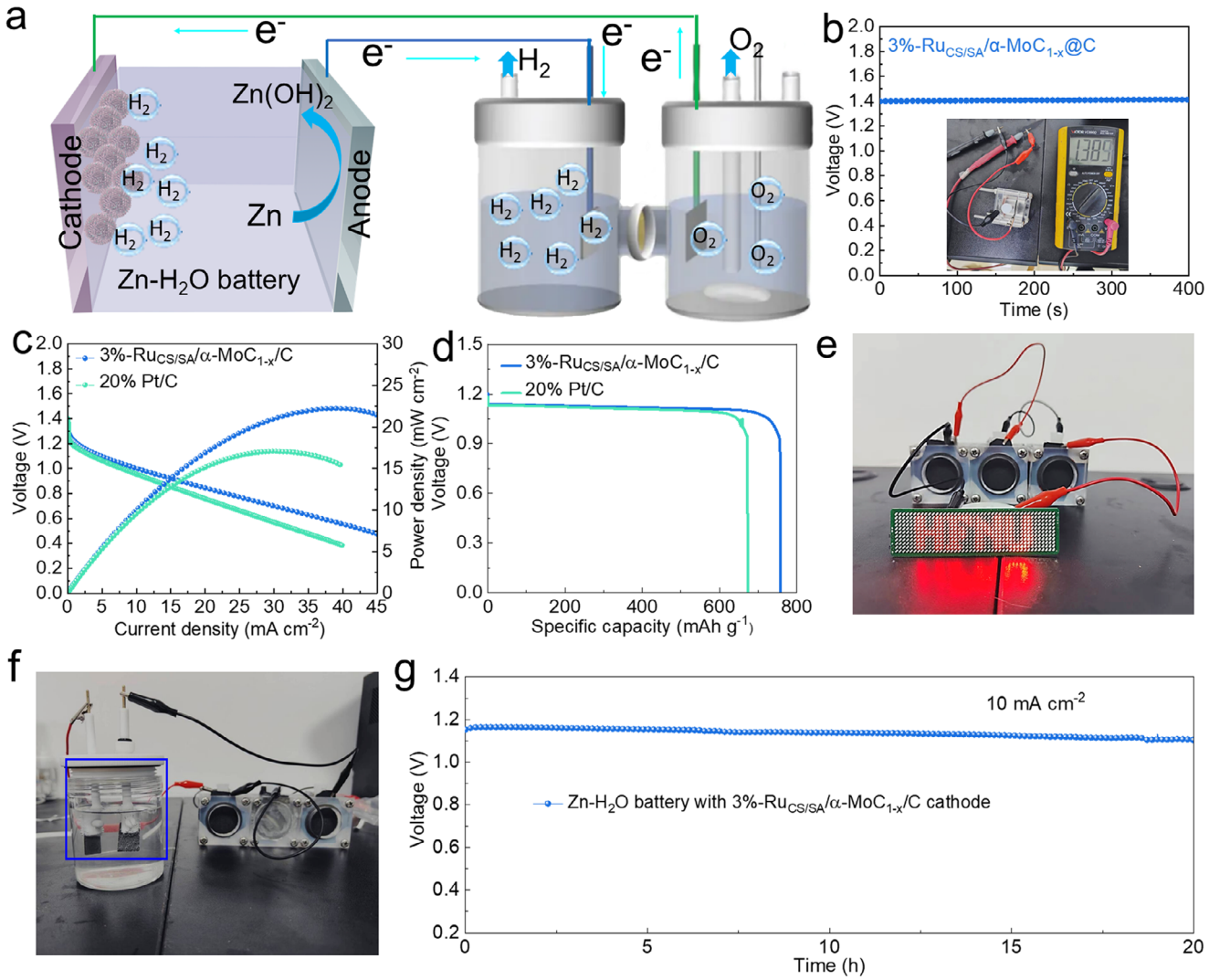

FIGURE 6 | a) Schematic illustration of the coupled configuration of double Zn–H_2O cells driving electrocatalytic water splitting. b) the open circuit potential (OCP) of 3%-$Ru_{CS/SA}$/α-MoC_{1-x}/C equipped Zn–H_2O cell. c) LSV curves (left-hand y axis) and power density (right-hand y axis) of 3%-$Ru_{CS/SA}$/α-MoC_{1-x}/C equipped Zn–H_2O cell. d) plot of voltage versus specific capacity of 3%-$Ru_{CS/SA}$/α-MoC_{1-x}/C and 20% Pt/C. e) the photograph of a dozen LEDs lightened by three as-assembled Zn–H_2O batteries with 3%-$Ru_{CS/SA}$/α-MoC_{1-x}/C cathode connected in series. f) Digital photograph of cathodic HER and anodic OER in the water electrolyzer powered by three Zn–H_2O fuel cells in series. g) Long-term durability tests for Zn–H_2O battery using 3%-$Ru_{CS/SA}$/α-MoC_{1-x}/C.

assigned to the orange (3225 cm^{-1}) and purple (3450 cm^{-1}) peaks, respectively. In contrast, the pink peak (3615 cm^{-1}), attributed to the free O-H bond of interfacial water, is associated with minimal HER activity due to weak interaction with catalyst surfaces [42]. Remarkably, 3%-$Ru_{CS/SA}$/α-MoC_{1-x}/C (Figure 4d) shows a faster decline in the pink peak intensity during HER compared to 1%-Ru_{SA}/α-MoC_{1-x}/C (Figure 4e). Moreover, the directly compared the Raman spectra of the two catalysts under identical potentials (Figure S43) can found that the O-H stretching band (≈3200–3600 cm^{-1}) is consistently stronger for the 3%-$Ru_{CS/SA}$/α-MoC_{1-x}/C than for the 1%-Ru_{SA}/α-MoC_{1-x}/C. The combination of the two indicates that enhanced water dissociation kinetics [43].

Quasi-in situ XPS combined with stage-by-stage XPS is used to monitor the dynamic evolution of the catalyst-electrolyte interface during the HER. This approach enables the observation of the evolution of different chemical species on the catalyst surface, which is essential to understanding the maintenance of high activity. As depicted in Figure 4f, the Mo 3d spectrum of the pre-reaction sample (0 V) exhibits three distinct peaks, while upon increasing the reaction potential from 0 to -70 mV, the peak at 228.5 eV undergoes a negative shift and intensity decrease. Additionally, the peak intensity of Mo-oxygenated species gradually decreases, indicating the further reduction of these species during HER. Consequently, the two peaks in the Ru 3p spectrum (Figure 4g) exhibit a negative shift (toward lower binding energy) as the potential increases from 0 to -30 mV, while remaining essentially unchanged between -40 and -70 mV. The stepwise measurements of the Mo 3d XPS (Figure 4h) and Ru 3p XPS (Figure 4i) show that after 15 h of reaction, the Mo 3d peak at 228.5 eV gradually disappears. Ru 3p shows a rightward shift within 15 h and then gradually stabilizes. Combining the changes of the two, we speculate that the reason for maintaining high activity is that the Ru species gain electrons, and the

electron-rich state of Ru is conducive to producing an ultra-strong HER process.

2.5 | Performance Evaluations of 3%-$Ru_{CS/SA}$/α-MoC_{1-x}/C in AEMWE Cells and Zn–H_2O Batteries

The AEMWE cells were constructed with 3%-$Ru_{CS/SA}$/α-MoC_{1-x}/C cathode and RuO_2 anode catalyst. The component of the AEMWE cell is depicted in Figure 5a. The polarization curves of the full cell with cathode catalysts (3%-$Ru_{CS/SA}$/α-MoC_{1-x}/C or commercial 20% Pt/C) and anode (the same commercial RuO_2) at 25°C are shown in Figure 5b. Notably, the AEM electrolyzer using 3%-$Ru_{CS/SA}$/α-MoC_{1-x}/C reached an industrial-level current density of 1000 mA cm^{-2} at an ultralow cell voltage of 2.08 V, much lower than the 2.42 V required by commercial 20% Pt/C at the same current density. Furthermore, the assembled cell (RuO_2(+) || 3%-$Ru_{CS/SA}$/α-MoC_{1-x}/C(-)) showed a significant performance enhancement at 60°C, delivering 1000 mA cm^{-2} at 1.78 V (Figure 5c), compared to 2.08 V at 25°C. Figure 5d and Figure S44 display the industrial current density curve of 1000 mA cm^{-2} at 60°C with 550 h of continuous operation, demonstrating that 3%-$Ru_{CS/SA}$/α-MoC_{1-x}/C is highly promising for AEMWE applications. Additionally, driven by such an exceptional HER activity of 3%-$Ru_{CS/SA}$/α-MoC_{1-x}/C, the integrated device was fabricated for enabling Zn–H_2O batteries to be used in energy storage and conversion. The reaction principle of the Zn–H_2O batteries is displayed in Figure 6a, which is assembled with as-prepared 3%-$Ru_{CS/SA}$/α-MoC_{1-x}/C as the cathode, a Zn plate as the anode, and 1 M KOH as the electrolyte. This configuration enables simultaneous power generation from the Zn oxidation reaction, leveraging the high HER activity of the cathode catalyst. As shown in Figure 6b, the alkaline Zn–H_2O batteries using 3%-$Ru_{CS/SA}$/α-MoC_{1-x}/C delivers a high open circuit potential (OCP) of 1.385 V. What is more, the assembled Zn–H_2O battery with a 3%-$Ru_{CS/SA}$/α-MoC_{1-x}/C cathode delivers a peak power density of 22.50 mW cm^{-2} (Figure 6c), markedly greater than the 17.20 mW cm^{-2} of the 20% Pt/C-based Zn–H_2O battery. Meanwhile, as shown in Figure 6d, the as-prepared battery exhibits a specific capacity of 760 mAh g^{-1}, outperforming the 690 mAh g^{-1} of the 20% Pt/C-based counterpart. Strikingly, LED strips (Figure 6e) are continuously illuminated by the integrated Zn–H_2O batteries based on 3%-$Ru_{CS/SA}$/α-MoC_{1-x}/C cathode. The integrated battery also enables the design of a self-feeding energy system for electrocatalytic water splitting (Figure 6f and Figure S45a). As presented in Figure S45b, the system delivers sufficient electrical energy to generate abundant bubbles attached to the cathode (3%-$Ru_{CS/SA}$/α-MoC_{1-x}/C for HER) and anode (RuO_2 for OER) in the reaction tank. In a separate battery system (Figure S46), the cathode spontaneously drives HER. The long-term discharge curve at 10 mA cm^{-2} (Figure 6g) displays that the battery maintains stable operation for 20 h, demonstrating its promising practical applications.

3 | Conclusions

In summary, Ru clusters with adjacent active Ru sites on the α-MoC_{1-x} substrate were synthesized via a facile pyrolysis strategy, serving as an efficient alkaline HER electrocatalyst. Driven by the ingenious nanoreactor architecture and distinct local charge redistribution between Ru single atoms/clusters and α-MoC_{1-x}. The as-prepared 3%-$Ru_{CS/SA}$/α-MoC_{1-x}/C catalyst demonstrates superior alkaline HER performance, requiring only 9 mV overpotential at 10 mA cm^{-2} and a low Tafel slope of 31.25 mV dec^{-1}. Moreover, it exhibits exceptional mass activity (20.38 A mg^{-1}_{Ru}) and TOF (1.71 s^{-1}) at -25 mV, alongside long-term stability (300 mA cm^{-2} for 110 h). Notably, an AEM electrolyzer using RuO_2(+) and 3%-$Ru_{CS/SA}$/α-MoC_{1-x}/C(-) operates continuously at an industrial current density of 1000 mA cm^{-2} for 550 h, significantly surpassing commercial 20% Pt/C. Meanwhile, the self-feeding Zn–H_2O battery system attains a power density of 22.50 mW cm^{-2} and is accompanied by stable discharging performance (10 mA cm^{-2}) for 20 h. This research not only offers a valuable strategy to synthesize efficient Ru-based catalysts but also expands our understanding of alkaline HER catalysis from a structure-activity perspective.

Acknowledgements

This work was financially supported by the National Key R&D Program of China (2017YFA0403503), the Excellent Research Innovation Team of Anhui Provincial Education Department (2023AH010001), the Natural Science Foundation of Anhui Province (2408085QE170), the Recruitment Program for Leading Talent Team of Anhui Province (LTIT20200002), the Key Projects of Natural Science Research in Universities of Anhui Province (2022AH052146, 2023AH051314, 2024AH051326), the Hefei Municipal Key Science and Technology R&D Program (2025SKJG-GHLG005), the Research Foundation for Talents of Hefei Institute of Technology (2025KY46), the National Natural Science Foundation of China (U25A20628, 22561160129, 22479074, 22475096), the Equipment Pre-Research and Ministry of Education Joint Fund (8091B02052407), the Fundamental Research Program Key Project of Jiangsu Province (BK20253008), the Science and Technology Major Project of Jiangsu Province (BG2024013), the Scientific and Technological Achievements Transformation Special Fund of Jiangsu Province (BA2023037), the Academic Degree and Postgraduate Education Reforming Project of Jiangsu Province (JGKT24_C001), the Key Core Technology Open Competition Project of Suzhou City (SYG2024122), the Open Research Fund of Suzhou Laboratory (SZLAB-1308-2024-TS005), and the Chenzhou National Sustainable Development Agenda Innovation Demonstration Zone Provincial Special Project (2023sfq11). We also thank XFNANO Materials Tech Co. Ltd. (Nanjing, China) for providing BN. The numerical calculations in this paper were performed by Hefei Advanced Computing Center.

Conflicts of Interest

The authors declare no conflicts of interest.

Data Availability Statement

The data that support the findings of this study are available from the corresponding author upon reasonable request.

References

1. R. Grinter, A. Kropp, H. Venugopal, et al., "Structural Basis for Bacterial Energy Extraction from Atmospheric Hydrogen," *Nature* 615 (2023): 541–547.

2. T. J. Wallington, M. Woody, G. M. Lewis, et al., "Green hydrogen pathways, energy efficiencies, and intensities for ground, air, and marine transportation,"*Joule* 8 (2024): 2190–2207.

3. C. Li, S. H. Kim, H. Y. Lim, et al., "Self-Accommodation Induced Electronic Metal–Support Interaction on Ruthenium Site for Alkaline Hydrogen Evolution Reaction," *Advanced Materials* 35 (2023): 2301369.

4. P. Kuang, Z. Ni, B. Zhu, Y. Lin, and J. Yu, "Modulating the D-Band Center Enables Ultrafine Pt_3 Fe Alloy Nanoparticles for pH-Universal Hydrogen Evolution Reaction," *Advanced Materials* 35 (2023): 2303030.

5. C. Wan, Z. Zhang, J. Dong, et al., "Amorphous Nickel Hydroxide Shell Tailors Local Chemical Environment on Platinum Surface for Alkaline Hydrogen Evolution Reaction," *Nature Materials* 22 (2023): 1022–1029.

6. T. Chao, W. Xie, Y. Hu, et al., "Reversible Hydrogen Spillover at the Atomic Interface for Efficient Alkaline Hydrogen Evolution," *Energy & Environmental Science* 17 (2024): 1397–1406.

7. J. Chen, C. Chen, M. Qin, et al., "Reversible Hydrogen Spillover in Ru-WO3-x Enhances Hydrogen Evolution Activity in Neutral pH Water Splitting," *Nature Communications* 13 (2022): 5382.

8. Y. Zheng, Y. Jiao, A. Vasileff, and S. Z. Qiao, "The Hydrogen Evolution Reaction in Alkaline Solution: from Theory, Single Crystal Models, to Practical Electrocatalysts," *Angewandte Chemie International Edition* 57 (2018): 7568–7579.

9. Z. Wu, Q. Li, G. Xu, et al., "Microwave Phosphine-Plasma-Assisted Ultrafast Synthesis of Halogen-Doped Ru/RuP_2 with Surface Intermediate Adsorption Modulation for Efficient Alkaline Hydrogen Evolution Reaction," *Advanced Materials* 36 (2024): 2311018.

10. D. Jeon, D. Y. Kim, H. Kim, N. Kim, C. Lee, and D. H. Seo, "Electrochemical Evolution of Ru-Based Polyoxometalates into Si,W-Codoped RuO X for Acidic Overall Water Splitting," *Advanced Materials* 36 (2024): 2304468.

11. Y. Li, W. Wang, M. Cheng, et al., "Arming Ru with Oxygen-Vacancy-Enriched RuO_2 Sub-Nanometer Skin Activates Superior Bifunctionality for pH-Universal Overall Water Splitting," *Advanced Materials* 35 (2023): 2206351.

12. Q. Hu, K. Gao, X. Wang, et al., "Subnanometric Ru Clusters with Upshifted D Band Center Improve Performance for Alkaline Hydrogen Evolution Reaction," *Nature Communications* 13 (2022): 3958.

13. J. Yang, B. Chen, X. Liu, et al., "Efficient and Robust Hydrogen Evolution: Phosphorus Nitride Imide Nanotubes as Supports for Anchoring Single Ruthenium Sites," *Angewandte Chemie* 130 (2018): 9639–9644.

14. Q. He, Y. Zhou, H. Shou, et al., "Synergic Reaction Kinetics over Adjacent Ruthenium Sites for Superb Hydrogen Generation in Alkaline Media," *Advanced Materials* 34 (2022): 2110604.

15. E. Liu, L. Jiao, J. Li, et al., "Interfacial Water Shuffling the Intermediates of Hydrogen Oxidation and Evolution Reactions in Aqueous Media," *Energy & Environmental Science* 13 (2020): 3064–3074.

16. J. Liu, S. Duan, H. Shi, et al., "Rationally Designing Efficient Electrocatalysts for Direct Seawater Splitting: Challenges, Achievements, and Promises," *Angewandte Chemie International Edition* 61 (2022): 202210753.

17. Q. He, D. Tian, H. Jiang, et al., "Achieving Efficient Alkaline Hydrogen Evolution Reaction over a Ni_5P_4 Catalyst Incorporating Single-Atomic Ru Sites," *Advanced Materials* 32 (2020): 1906972.

18. H. Zhang, K. Song, Z. Lin, et al., "In Situ Reconstructed Ru Clusters on LaRuSi 3 with Enhanced Electrocatalytic Activity for Alkaline Hydrogen Evolution," *Advanced Functional Materials* 34 (2024): 2405897.

19. J. Zhang, J. Ma, T. S. Choksi, et al., "Strong Metal–Support Interaction Boosts Activity, Selectivity, and Stability in Electrosynthesis of H_2O_2," *Journal of the American Chemical Society* 144 (2022): 2255–2263.

20. J. Zhou, Z. Gao, G. Xiang, et al., "Interfacial Compatibility Critically Controls Ru/TiO_2 Metal-Support Interaction Modes in CO2 Hydrogenation," *Nature Communications* 13 (2022): 327.

21. T. Pu, W. Zhang, and M. Zhu, "Engineering Heterogeneous Catalysis with Strong Metal–Support Interactions: Characterization, Theory and Manipulation," *Angewandte Chemie International Edition* 62 (2023): 202212278.

22. X. Zhang, M. Zhang, Y. Deng, et al., "A Stable Low-Temperature H2-Production Catalyst by Crowding Pt on α-MoC," *Nature* 589 (2021): 396–401.

23. H. D. Mai, S. Jeong, G. N. Bae, et al., "Pd Sulfidation-Induced 1T-Phase Tuning in Monolayer MoS_2 for Hydrogen Evolution Reaction," *Advanced Energy Materials* 13 (2023): 2300183.

24. X. Zhou, Y. Tian, J. Luo, et al., "MoC Quantum Dots@N-Doped-Carbon for Low-Cost and Efficient Hydrogen Evolution Reaction: from Electrocatalysis to Photocatalysis," *Advanced Functional Materials* 32 (2022): 2201518.

25. L. Lin, W. Zhou, R. Gao, et al., "Low-Temperature Hydrogen Production from Water and Methanol Using Pt/α-MoC Atalysts," *Nature* 544 (2017): 80–83.

26. W. Wang, Y. Wu, Y. Lin, et al., "Confining Zero-Valent Platinum Single Atoms in α-MoC 1−X for pH-Universal Hydrogen Evolution Reaction," *Advanced Functional Materials* 32 (2022): 2108464.

27. N. Tang, D. Liu, S. Chen, et al., "Pt Atom-Substituted MoC Single-Atom Catalyst for Enhancing H 2 Production," *ACS Catalysis* 14 (2024): 14297–14307.

28. X. Fan, C. Liu, M. Wu, et al., "Synergistic Effect of Dual Active Sites over Ru/A-Moc for Accelerating Alkaline Hydrogen Evolution Reaction," *Applied Catalysis B: Environmental* 318 (2022): 121867.

29. J. Guo, R. Ding, Y. Li, et al., "Semi-Ionic F Modified N-Doped Porous Carbon Implanted with Ruthenium Nanoclusters toward Highly Efficient pH-Universal Hydrogen Generation," *Small* (2024): 2403151.

30. C. H. Chen, D. Wu, Z. Li, et al., "Ruthenium-Based Single-Atom Alloy with High Electrocatalytic Activity for Hydrogen Evolution," *Advanced Energy Materials* 9 (2019): 1803913.

31. R. Dronskowski and P. E. Blöchl, "Crystal Orbital Hamilton Populations (COHP): Energy-Resolved Visualization of Chemical Bonding in Solids Based on Density-Functional Calculations," *The Journal of Physical Chemistry* 97 (1993): 8617–8624.

32. J. K. Nørskov, T. Bligaard, A. Logadottir, et al., "Trends in the Exchange Current for Hydrogen Evolution," *Journal of The Electrochemical Society* 152 (2005): J23.

33. Y. Han, L. Zhao, W. Cheng, et al., "Iridium Cluster Anchored onto Cubic Molybdenum Carbide with Strong Electronic Interactions for Robust Hydrogen Oxidation Reaction in Alkaline Medium," *Advanced Functional Materials* 34 (2024): 2407060.

34. K. Jiang, B. Liu, M. Luo, et al., "Single Platinum Atoms Embedded in Nanoporous Cobalt Selenide as Electrocatalyst for Accelerating Hydrogen Evolution Reaction," *Nature Communications* 10 (2019): 1743.

35. P. Su, W. Pei, X. Wang, et al., "Exceptional Electrochemical HER Performance with Enhanced Electron Transfer between Ru Nanoparticles and Single Atoms Dispersed on a Carbon Substrate," *Angewandte Chemie* 133 (2021): 16180–16186.

36. G. Fang, C. Liu, M. Xu, et al., "The Elaborate Design of Multi-Polarization Effect by Non-Edge Defect Strategy for Ultra-Broad Microwave Absorption," *Advanced Functional Materials* 34 (2024): 2404532.

37. Z. Jiang, R. Yuan, Z. Jiang, et al., "Utilizing Ultra-homogeneous SiOx and Defects to Achieve Interlayer Protection for Lithium Metal Anodes," *Small* 19 (2023): 2303294.

38. Y. Wu, S. Tan, G. Fang, Y. Zhang, and G. Ji, "Manipulating CNT Films with Atomic Precision for Absorption Effectiveness–Enhanced Electromagnetic Interference Shielding and Adaptive Infrared Camouflage," *Advanced Functional Materials* 35 (2024): 2402193.

39. C. Yang, Z. Wu, Z. Zhao, et al., "Mn-Oxygen Compounds Coordinated Ruthenium Sites with Deprotonated and Low Oxophilic Microenviron-

ments for Membrane Electrolyzer-Based H 2 -Production," *Advanced Materials* 35 (2023): 2303331.

40. J. Yu, A. Wang, W. Yu, et al., *Applied Catalysis B: Environmental* 277 (2020):119236 .

41. Q. Dai, L. Wang, K. Wang, et al., "Accelerated Water Dissociation Kinetics by Electron-Enriched Cobalt Sites for Efficient Alkaline Hydrogen Evolution," *Advanced Functional Materials* 32 (2022): 2109556.

42. Y. Zhang, R. Li, X. Wang, et al., "Surface Active-Site Engineering of Low-Noble-Metal-Alloyed Metallic Glass Catalyst for Boosting Water Electrolysis," *Advanced Functional Materials* 34 (2024): 2410379.

43. Y. Zhu, M. Klingenhof, C. Gao, et al., "Facilitating Alkaline Hydrogen Evolution Reaction on the Hetero-Interfaced Ru/RuO_2 through Pt Single Atoms Doping," *Nature Communications* 15 (2024): 1447.

Supporting Information

Additional supporting information can be found online in the Supporting Information section.

Supporting file: adma71934-sup-0001-SuppMat.docx